Advanced Steel Construction – Vol. 20 No. 4 (2024) 364–375
DOI:10.18057/IJASC.2024.20.4.4

MECHANICAL PROPERTIES OF ASSEMBLED WALL-SLAB JOINTS BETWEEN THIN DOUBLE SKIN COMPOSITE SHEAR WALLS AND PRECAST FLOOR SLABS SUBJECTED TO PURE BENDING

Jie Liu [1, 2], Zhi-Hua Chen [1], Ting Zhou [3, *] and Xiao-Feng Wang [2, 4]

[1] *School of Civil Engineering, Tianjin University, Tianjin, 300072, China*
[2] *Central Research Institute of Building and Construction Co., Ltd, MCC Group, Beijing 100088, China*
[3] *School of Architecture, Tianjin University, Tianjin, 300072, China*
[4] *National Steel Structure Engineering Technology Research Center, Beijing 100088, China*
** (Corresponding author: E-mail: zhouting1126@126.com)*

ABSTRACT

Two new types of assembled wall-slab joints are proposed for thin double skin composite shear walls and steel truss floor slabs, which are commonly used in construction. Pure bending tests were performed to investigate the failure modes and mechanical performance of these newly devised wall-slab joints. The results demonstrated that the new assembled wall-slab joints offer superior flexural bearing capacity and ductility. When subjected to pure bending load, the steel truss floor slabs failed before the joints, adhering to the design principle of "strong joints and weak members". Finite element models for the new assembled wall-slab joints were established and compared with test results. Furthermore, recognizing the prefabricated floor slab's failure section as the weakest, a new formula to calculate the bending capacity of these wall-slab joints was proposed, based on the principle of sectional force balance. Notably, these calculated results were more conservative than the test results.

ARTICLE HISTORY

Received: 27 October 2023
Revised: 30 August 2024
Accepted: 5 September 2024

KEYWORDS

Assembled wall-slab joints;
Thin double skin composite shear wall;
Pure bending test;
Finite element model;
Calculation method

1. Introduction

Owing to high population density and limited land resources, many urban areas in China have experienced an increase in the height of residential buildings to conserve urban land and accommodate large populations. As the height of these buildings increases, their structural sensitivity to lateral loads, such as seismic and wind forces, becomes more pronounced. Shear wall systems, which comprise rigidly connected shear walls and floor slabs, effectively counteract these lateral loads and are commonly employed in high-rise construction[1]. Previous studies have identified that the highest stress concentrations occur at the joints between shear walls and slabs under seismic loads. The primary failure mode in these joints is often attributed to inadequate ductility, resulting from improper arrangement in the joint zones, which can lead to potential global structural failures[2]. Consequently, numerous scholars have conducted extensive experimental research on traditional shear wall-to-slab joints and proposed more detailed reinforcement strategies[3-7]. These strategies include dual-layer reinforcement within the wall, additional transverse reinforcement, external FRP grid reinforcement, cross bracing, and X-type reinforcements, among others. These methods have been demonstrated to significantly enhance the load-bearing performance of these joints.

In the realm of prefabricated construction, the safety of joints between precast shear walls and floor slabs becomes paramount. Precast reinforced concrete shear walls are typically manufactured in factories and assembled on-site using wet joints at wall-to-slab interfaces. To enhance the bond characteristics in the core areas of these joints, reinforcing bars from the slabs are anchored within the shear walls. The entire assembly is made to work as a unit once the cast-in-place concrete reaches the desired strength[8]. Comparative studies between precast and cast-in-place joints have confirmed the structural integrity of prefabricated wall-to-slab joints[9-12].

Additionally, double skin composite (DSC) shear walls, a prevalent structural form in prefabricated construction, are widely used in nuclear facilities and high-rise buildings due to their high load-bearing capacity, superior seismic performance, and construction ease[13-15]. Per the Chinese code "Technical Specification for Steel Plate Shear Walls" [16], steel plates in commonly used shear walls are recommended to be at least 10 mm thick, with an optimal thickness ratio between the wall body and steel plates ranging from 25 and 100. Therefore, the minimum thickness of commonly used DSC shear wall is 250mm. However, in an effort to maximize indoor space, developers are increasingly reducing the thickness of shear walls, prompting researchers to develop innovative forms of thin DSC shear walls[17-20]. Studies indicate that, even with reduced wall thickness, these walls maintain a high load-bearing capacity and stiffness, and their seismic performance remains robust[18]. The interior of the thin DSC shear walls is segmented into channels with smaller cross-sectional areas, facilitating the integration of transverse reinforcements within the specimens, significantly enhancing their strength[17].

Common connection techniques for DSC shear walls with cast-in-place floor slabs involve reserving anchoring steel bars and shear connectors at the wall ends, followed by welding floor slab rebars to these anchors before pouring concrete[21]. Assembly methods for precast composite floor slabs and shear walls may similarly follow these procedures. However, installing precast composite floor slabs requires reliable support from below, which complicates construction. Despite numerous patents filed on the connections between steel plate shear walls and precast composite floor slabs, mechanical performance tests remain scarce, leaving the reliability of these connections unverified. Consequently, this study introduces two new types of assembly connection connections between thin DSC shear walls and prefabricated floor slabs. Compared to existing connection types, these improvements directly support the composite floor slabs on the lower flanges of angle or H-shaped steel, thereby simplifying construction and enhancing convenience.

To investigate the connection performance of thin DSC shear walls and prefabricated floor slabs, the steel truss floor slab is utilized, as shown in Fig. 1. The steel truss comprises upper rebars, lower rebars and web rebars, assembled through spot welding. Comprising the steel truss and the composite plate, together with the cast-in-place concrete above, forms a complete steel truss floor slab. The composite plate can be used as the formwork for pouring concrete and can bear the weight of concrete and certain construction loads during the construction stage. The steel truss floor slab is widely used in China towing to its standardization, high load-bearing capacity, and ease of construction.

In this study, we introduce two new types of assembled wall-slab joints for thin double skin composite shear walls and steel truss floor slabs. A pure bending test of these two types of new assembled wall-slab joints is conducted. The failure modes and mechanical properties of these newly assembled wall-slab joints across various joint forms and slab thicknesses were investigated. Using the ABAQUS finite element platform, finite element models of the new assembled wall-slab joints is established and compared the simulation results with the test outcomes to evaluate the modeling method's feasibility. A method for calculating the pure flexural bearing capacity of the joints, based on the stress balance of the broken section of the specimen is proposed. The finding of this research may serve as a reference for applying the new assembled wall-slab joints in engineering practices and for predicting the joints' bearing capacity.

Fig. 1 Steel truss floor slab

2. Experimental study

Two types of assembled wall-slab joints, Type I and Type II, were tested. In the construction of the Type I, an angle steel is affixed to the shear wall, with the prefabricated floor slabs subsequently placed atop the angle steel. Anchorage steel bars are threaded through both the shear wall and floor slab. The process concludes with the pouring of the floor concrete. For the Type II joint, an H-shaped steel with unequal upper and lower flanges is welded to the shear walls, and the lower flange of the H-shaped steel supports the prefabricated floor slabs. Similarly, the anchorage steel bars are threaded through the shear wall, H-shaped steel and the floor slab. This assembly concludes with the pouring of the floor concrete. These two types of joints obviate the need for traditional bottom formwork and support frame in concrete floor slabs, thereby optimizing process flow and accelerating assembly speed. Anchored steel bars are strategically positioned in the tension area of the joints to counteract the tensile stresses induced by bending moment. Due to structural design considerations, the anchoring reinforcement bars in the Type I joint may be positioned either above (Fig. 2a) or below (Fig. 2b) the upper rebars of the slab, leading to variable floor thickness. Consequently, this study produced three joint specimens: two angle-steel joints (Type I), namely CWSA140 (Fig. 2a) and CWSA120 (Fig. 2b), and one H-steel joint (Type II), labeled CWH130 (Fig. 2c).

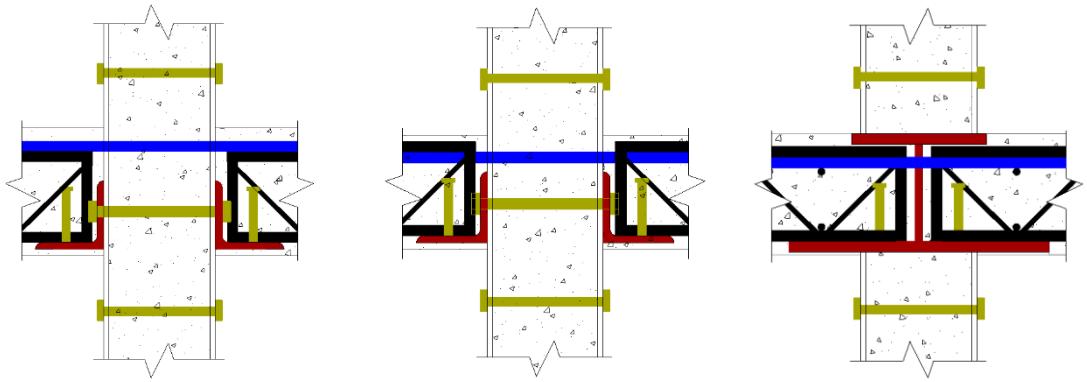

(a) CWSA140 (b) CWSA120 (c) CWH130

Fig. 2 Structure of joints of DSC shear wall and stee truss floor slab

2.1. Specimen design

Three assembled wall-slab joints have been designed for thin DSC shear walls and steel truss floor slabs. The DSC shear wall features a width of 130 mm, steel plate thickness of 6 mm on both sides, and is infilled with C30 concrete. The composite floor slab comprises a steel bar truss deck, model TD7-90, produced by Duowei Union Group Co., Ltd. The floor slab incorporates three trusses, each 90 mm high and 100 mm wide, spaced 100 mm apart. The upper and lower rebars of the steel truss have a diameter of 12 mm, while the web rebars measure 5.5 mm in diameter. The steel plate, angle steels, and H-steel are composed of Q345B steel, whereas the steel bar utilizes HRB400. The shear bolt specification is M16×80. The anchoring reinforcement bars measure 10 mm in diameter and 400 mm in length, extending into the floor slab. Each specimen contains three anchorage bars, spot-welded with the upper rebars of the steel truss. The tension bolts on the shear walls are spaced300 mm apart and have a diameter of 10 mm. Detailed sizes of the specimens are provided in Table 1, and their structure is illustrated in Fig. 3. The thickness of the concrete protective layer is 15mm. Distance between the hinged support and both ends of the specimen is 200 mm.

2.2. Material properties

Six cubic concrete test blocks (150 mm × 150 mm × 150 mm) were prepared, and a cube compression test was performed after 28 days of curing. The measured compressive strength of the concrete cubes was 35.65 MPa. According to the “Metal Materials tensile test method at room temperature” guidelines, the yield strength, tensile strength, and elastic modulus of various steels were measured (Table 2). The material testing results for the steel and concrete are presented in Figs. 4 and 5.

Table 1
Statistics of pure bending specimens

Group	Specimen number	Shear wall size T × B × H/mm	Single slab length L/mm	Slab thickness t/mm	SA/HB size/mm	Total length L/mm
Type I	CWSA140	130×500×600	1600	140	60×80×8×8	3330
	CWSA120	130×500×600	1600	120	60×80×8×8	3330
Type II	CWH130	130×500×600	1600	130	124×290（150）×10×12	3330

Table 2
Properties of steel and concrete materials

Name	Thickness t/mm	Yield strength f_y (MPa)	Ultimate strength f_u (MPa)	Modulus of elasticity E
Steel plate	5.8	389.58	569.42	205045.82
Steel angle	8.2	390.43	541.36	205292.88
Upper rebar /Lower rebar/ anchorage rebar	12	425.49	599.38	183110.96
Web rebar	10	254.07	523.43	181384.68
Compressive strength of concrete	f_c=35.65Mpa			

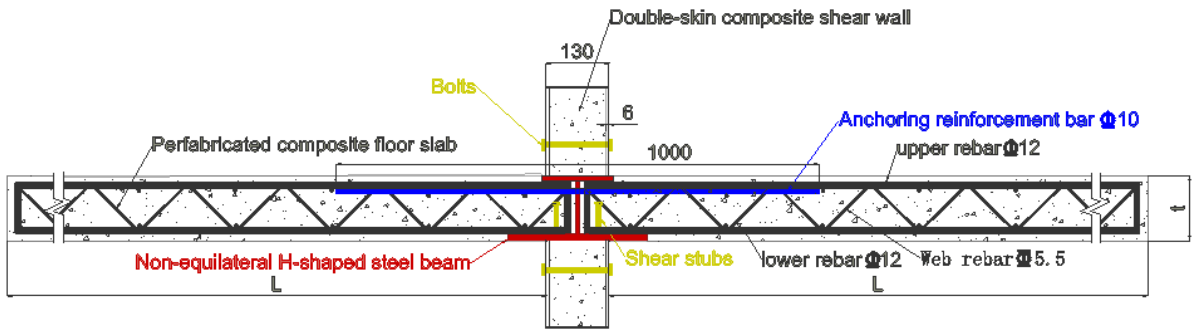

(a) Front view of the overall structure

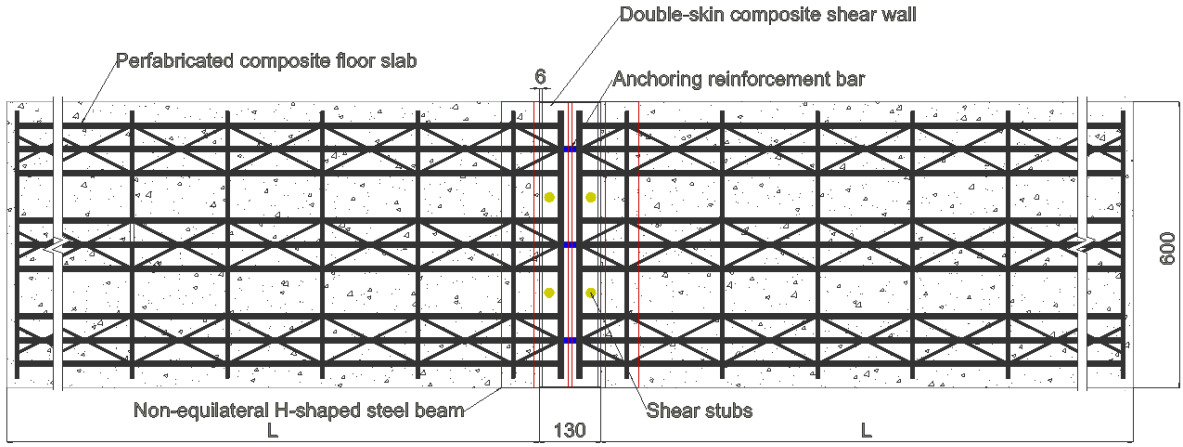

(b) Vertical view of the overall structure

Fig. 3 Specimen size and overall structure (taking Type II joint as an example)

(a) Loading device

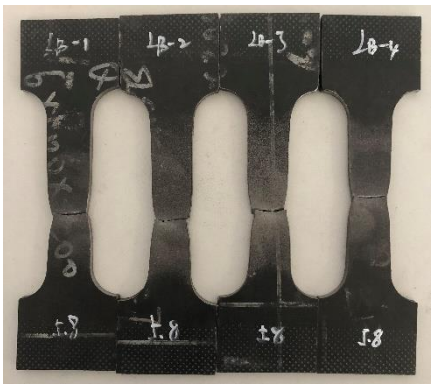

(b) Steel plate and SA specimens

(c) Reinforcement bar specimens

Fig. 4 Properties test of steel materials

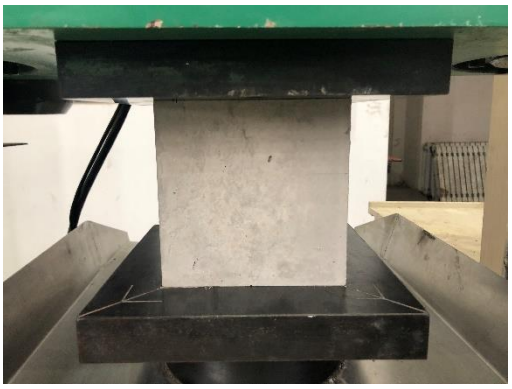

(a) Loading device

(b) Concrete specimens

Fig. 5 Properties test of concrete materials

2.3. Test device and measurement

In the Civil Structures Laboratory of Tianjin University, a laboratory reaction frame, sensors, and an MTS electro-hydraulic servo loading device (Fig. 6) were utilized to conduct the pure bending tests on newly assembled wall-slab joints. The orientation of the joint specimens, depicted in Fig. 2, was initially set in a regular placement direction. Under bending moment load, the lower part of the joint experiences compressive stress while the upper part undergoes tensile stress. During testing, to simulate the actual stress conditions experienced in practical applications, the specimens were rotated 180 degrees (Fig. 6). A vertical load was applied downward along the length direction of the specimen at two points, one-quarter of the way from each end, to mirror the load distribution typical in engineering application. For descriptive supposes, the directions of the specimen were labelled as N- and S-directions. Side A represented the compression surface, side B faced the tension surface, side D faced the tester, and side C was oriented opposite to the tester.

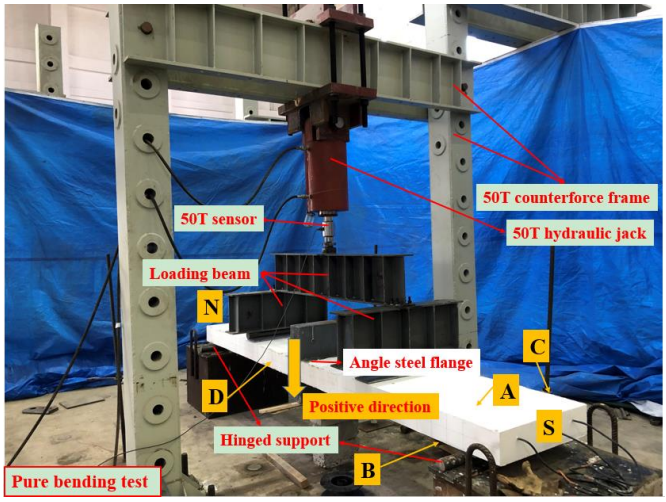

Fig. 6 Loading device of pure bending test

2.4. Measuring arrangement and loading system

Principal positions were identified for measuring strain and deformation in the specimens. Fig.7 and Fig.8 illustrate the arrangement of the strain gauge and linear variable displacement transducers (LVDTs) on the specimens. The pure bending test was a unidirectional static loading test. In the preloading stage, 10% of the initial calculated cracking load was applied in five incremental stages, with each stage maintained for one min. This stage was followed by verifying the working status and connection of the instrument, and the familiarity of the operators. It was then unloaded to zero. A grading loading system was adopted during formal loading, and 10% of the calculated yield load was loaded at each stage, and 5% of the yield load was controlled when it was close to the ultimate load. The test was stopped when the load was directly loaded to 80% of the ultimate load or the peak load or the crack width of the concrete reached 10 mm.

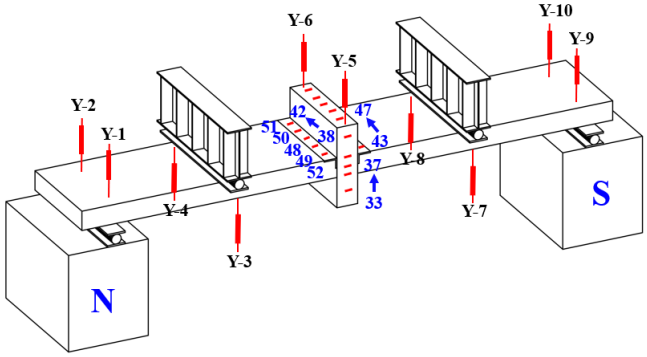

Fig. 7 Strain gauge and LVDTs of pure bending test

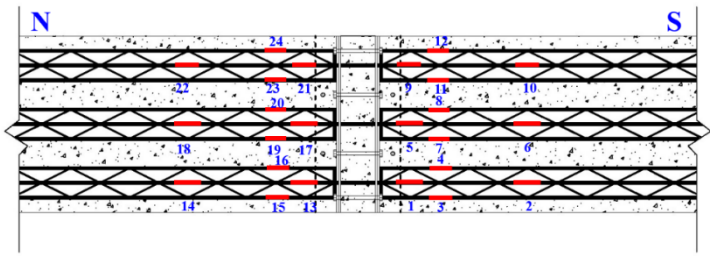

Fig. 8 Reinforcement strain gauge arrangement

3. Results and analysis

3.1. Test phenomenon

The test procedure was divided into three stages.

(1) Elastic Working Stage to Tensile Zone Concrete Cracking Stage. Initially, all sections exhibited minimal bending moments, and the specimens remained in an elastic working state. As the load escalated, the first crack appeared approximately 150 mm from the loading point within the slab's tension zone. Comparing the cracking load of different specimens, it can be found that specimen CWSA140 was the first to crack, while specimen CWH130 demonstrated the greatest resistance, cracking last.

(2) Tensile Zone Concrete Cracking Stage to Longitudinal Tension Reinforcement Yield Stage. As the load increased, cracks in the slabs proliferated and propagated from the tension zone to the compression zone along the slab height. Crack began to propagate at 45-degree angle on both sides, and the rate of crack width expansion accelerated. Significant deflection was observed as the specimens reached the yield load. Cracks within the tensile zone were evenly distributed across the bending zone along the slab length.

(3) Longitudinal Tension Reinforcement Yield Stage to Failure Stage. Subsequent to the longitudinal tension reinforcement yielding, a noticeable inflection point was observed in the load-displacement curve of the specimens, with specimen deflections increasing rapidly. Specimens CWSA140, CWSA120 and CWH130 failed upon reaching vertical displacements of 99, 173, and 110 mm, respectively. The failure points were all located within the concrete's compression zone, 150 mm away from the loading point in the S-direction. Despite the increase in load, the number of cracks stabilized, but their width expanded significantly. As specimen CWSA140 reached the ultimate load, the bearing capacity declined abruptly, accompanied by the audible snap of the reinforcing bar. The bearing capacity of specimen CWSA140 initially increased with continuous loading due to stress redistribution within the force section, before eventually declining. A significant cracking sound was noted as the vertical displacement of specimen CWSA140 reached 155 mm, which was immediately followed by the emergence of a substantial crack at the loading end in the S direction and a sharp decline in bearing capacity, signalling the conclusion of the test. For specimen CWSA120, the slab cracked and the bearing capacity plummeted when the vertical displacement reached 183 mm. The slab of specimen CWH130 fractured with a loud noise upon reaching the ultimate load of 49.31 kN, reducing its bearing capacity to zero.

After the test, all specimens demonstrated significant deflections, with a extensive crack in the S-direction of the three slabs (Fig. 9). The maximum crack widths at the final failure stage for specimens CWSA140, CWSA120, and CWH130 were recorded as 5 mm, 10 mm, and 2 mm, respectively. Notably, the deformation resistance of the H-steel joint (CWH130) exceeded that of the angle-steel joints (CWSA140 and CWSA120). Damage within the mid-span joint region of all three specimens was depicted in Fig. 9. In specimen CWSA140, cracks originated at the interface between the shear wall and the floor slab at the base, ascending along the interface. These cracks ascended along the contact surface, halting at the angle flange (Fig. 10a). Simultaneously, the concrete floor slab near the specimen's loading point sustained crushing and damage. The crack development in the joint area of specimen CWSA120 was mirrored that of specimen CWSA140. After the tensile zone's concrete cracking, anchored rebars underwent tensile stress. Since the anchoring reinforcement bars of the angle-steel joints (CWSA120 and CWSA140) were positioned differently, the anchoring reinforcement bars of CWSA120 were only activated when the concrete cracks were substantial. Consequently, the deformation capacity of CWSA120 was inferior to that of CWSA140, resulting in more extensive crack development in the joint area (Fig. 10b). The anchorage bars in the joint area of specimen CWH130 extended into the H-shaped steel's interior, thereby preserving the joint area's integrity. Cracks that appeared in CWH130 during the initial loading stage did not expand in the subsequent stages (Fig. 10c).

(a) Deformation and bottom cracks (b) Deformation and concrete fracture

Fig. 9 Overall deformation of the three specimens

(a) CWSA140 (b) CWSA120 (c) CWH130

Fig. 10 Local failure of the three specimens

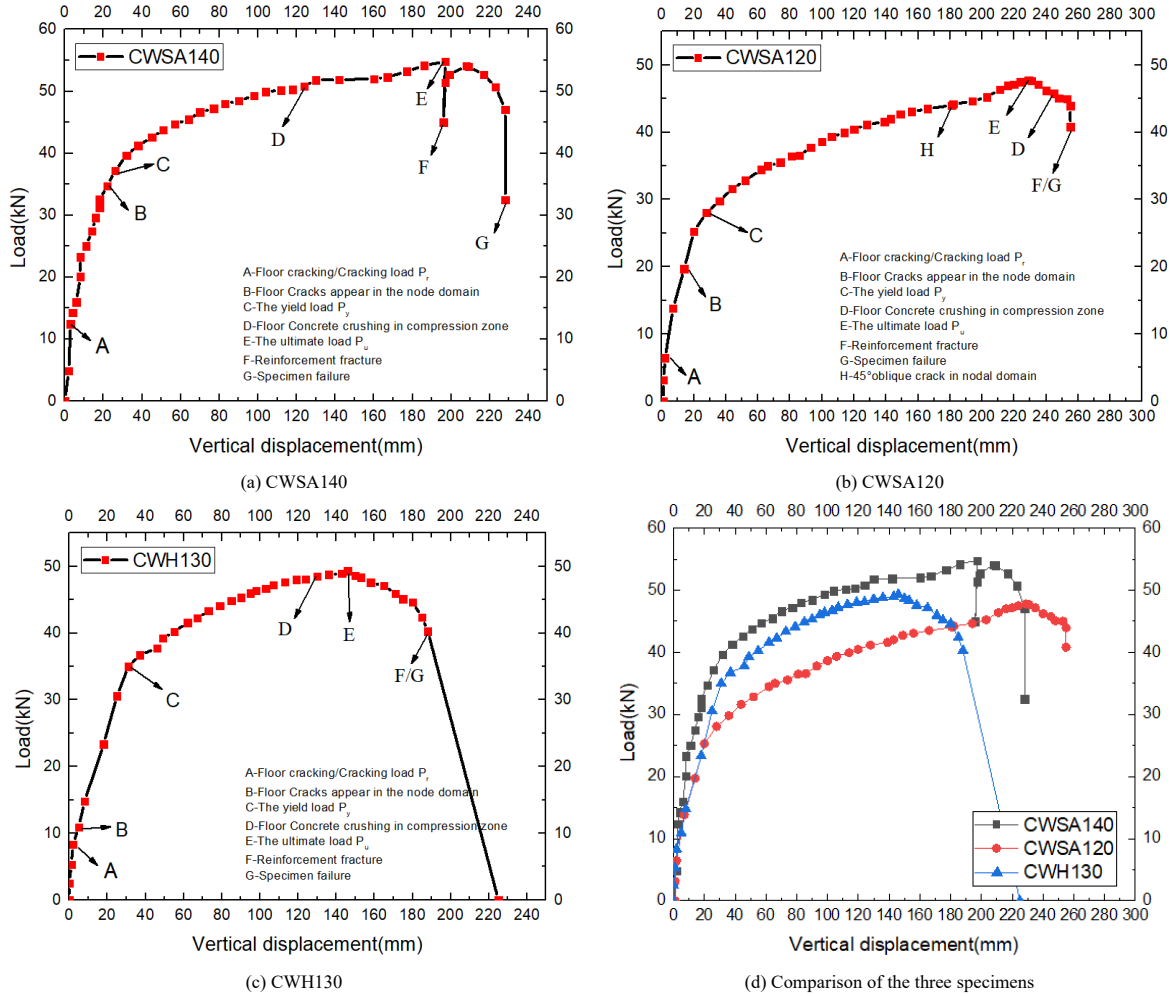

(a) CWSA140 (b) CWSA120

(c) CWH130 (d) Comparison of the three specimens

Fig. 11 Load–displacement curves

3.2. Load–displacement curve

Fig.11 presents a comparison of the load–displacement curves for the three specimens. The load was measured using a 50 T sensor coupled with a static acquisition instrument. The vertical displacement was calculated by averaging the readings from of LVDTs Y-5 and Y-6. Key points on each load–displacement curve was highlighted to emphasize specific characteristics.

The specimen CWSA140 exhibited the greatest initial stiffness and ultimate load. Upon achieving its ultimate load, the bearing capacity of specimen CWSA140 experience a significant reduction. This abrupt decrease can be primarily attributed to the breakage of the slab tensile rebars at the loading beam in the S-direction. Despite additional load increments, the concrete in the slab's tensile area continued to disengage from the applied load, culminating in the steel rebars at the crack reaching their capacity limit. As the crack width expanded, the bearing capacity of specimen CWSA140 declined rapidly. When specimens CWSA120 and CWH130 reached their ultimate bearing capacity, there was a continuous increase in the crack width in the slab's tensile zone at the loading end in S direction. Following the fracture of the tensile rebars, the bearing capacity of the two specimens decreased rapidly and could no longer sustain additional load. Due to safety concerns, the tests were terminated at this juncture.

Compared to specimen CWSA120, the ultimate load of specimen CWSA140 increased by 14.72%, and the ultimate displacement decreased by 13.93%. This variationist primarily attributed to the different placements of the anchorage rebars. In specimen CWSA140, the arrangement of anchorage rebars not only increased the section height of the sla but also enhanced its flexural stiffness. In comparison to specimen CWSA120, the initial stiffness of specimen CWH130 improved, the ultimate load increased by 3.27%, and the ultimate displacement decreased by 36.02%. Although specimen CWH130 exhibited earlier cracking compared to the SA connection specimens, the progression of these cracks was more gradual. The angle-steel joints specimens developed cracks at a later stage, yet these exhibited larger final crack widths compared to those in the H-steel joint specimen.

The ductility and deformation capacity of the test specimens were evaluated by analysing the ductility coefficient and the rotation capability. All three specimens demonstrated ductility coefficients exceeding 5, indicative of superior ductility in the connections between the DSC shear wall and the steel truss floor slab. Notably, specimen CWSA120 exhibited the lowest bearing capacity yet excelled remarkable ductility. The ratio of the ultimate bearing capacity to the yield bearing capacity (P_p/P_y) of all three specimens ranged between 1.47-1.89. This data suggests that the flexural bearing capacity of these assembled wall-slab joints possesses a substantial safety margin. Additionally, the peak angle θ_p of all specimens exceeded 1/10, demonstrating the robust deformation ability of these assembled wall-slab joints.

Here, P_y and Δ_y represent the yield load and yield displacement, respectively, P_p and Δ_p represent the peak load and peak displacement, respectively, θ_y and and θ_p represent the floor rotation under yield load and peak load, respectively, μ represents the ductility coefficient.

Table 3
Characteristics of each specimen

Specimens	P_y/kN	Δ_y/mm	θ_y	P_p/kN	Δ_p/mm	θ_p	μ	P_p/P_y
CWSA140	37.16	26.64	1/52	54.78	197.12	1/5.5	7.4	1.47
CWSA120	25.26	20.33	1/62	47.75	229.01	1/4	11.26	1.89
CWH130	30.56	24.87	1/34.4	49.31	146.52	1/13.5	5.89	1.61

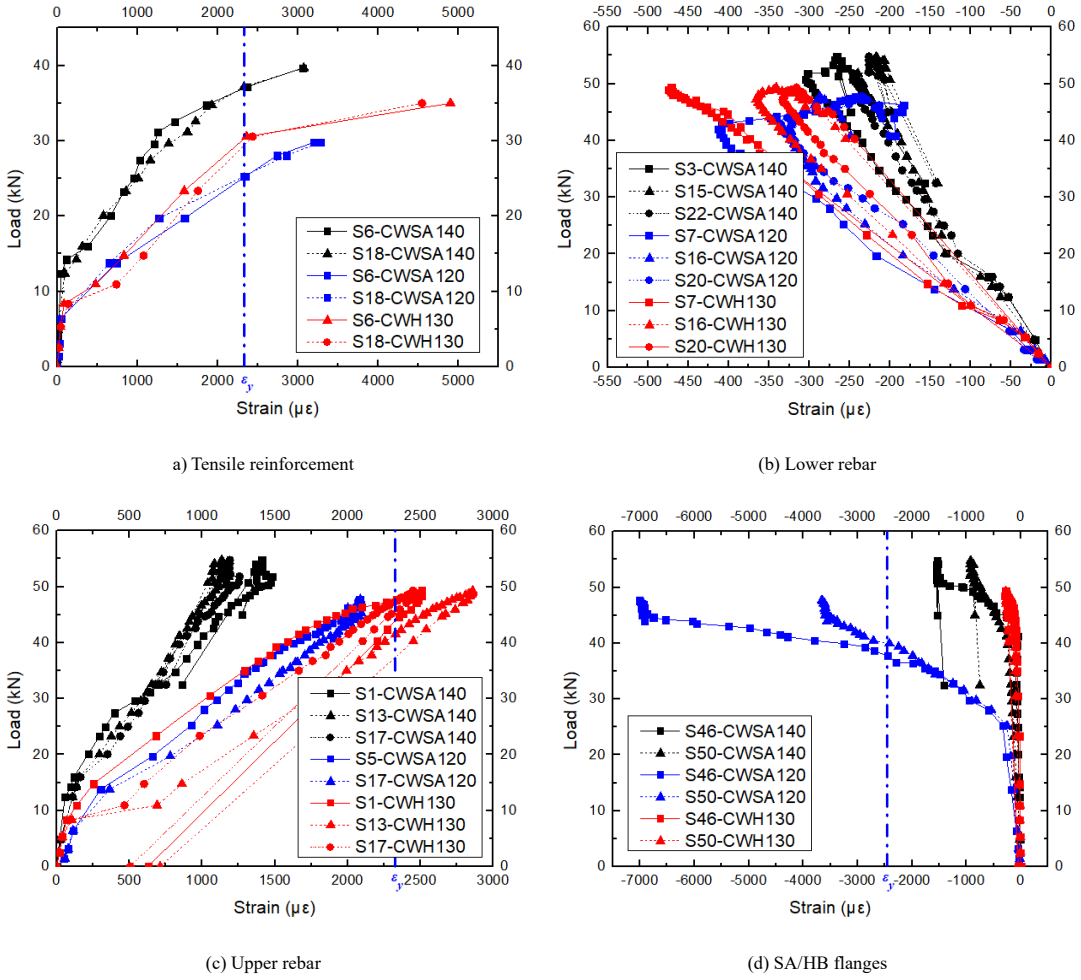

a) Tensile reinforcement (b) Lower rebar

(c) Upper rebar (d) SA/HB flanges

Fig. 12 Strain analysis of specimens

3.3. Strain analysis

Fig. 12 illustrates the load-strain curves for the three specimens. The upper rebars of the steel truss at the loading point reached the yield stress in all specimens, which is consistent with the observed fracture positions. Conversely, the lower rebars of the steel truss, which were subjected to compressive stress, did not yield at the ultimate load. Notably, strain development in the upper rebars within the tensile zone near the joint area was significantly slower than at the loading point. Upon reaching the ultimate load, the tensile rebars in the joint zone of specimens CWSA140 and CWSA120 did not yield, while those in the joint tension zone of specimen CWH130 reached the yield stress. This behavior, coupled with the failure phenomena observed in the joint areas (Fig. 10), demonstrates that the joint structure of the CWH130 specimen is more logical and effective. The anchoring rebars in specimen CWH130 proved effectively anchoring the two prefabricated floor slabs and shear walls, thereby efficiently transmitting the negative bending moment of the floor slab.

4. Finite element analysis

4.1. Finite element modeling

Finite element models for the newly assembled wall-slab joints of thin double skin composite shear walls and steel truss floor slabs were developed using the ABAQUS finite element platform. Based on tensile test results of steel plates and rebars, the constitutive models of all steel components were simplified. The simplified constitutive model of steel plate and rebars adopted the elastoplastic stress-strain relation model proposed by Han et al, as indicated in Fig. 13(a). The stress-strain relation model of concrete adopted the constitutive relation proposed by in Appendix C of the Code for Design of Concrete Structures[22], as indicated in Fig. 13(b). Additionally, the damage plasticity model defined in ABAQUS was used to simulate the three-way force relationship in the concrete of shear wall and slabs. Key material parameters were determined according to previous studies[23-25].

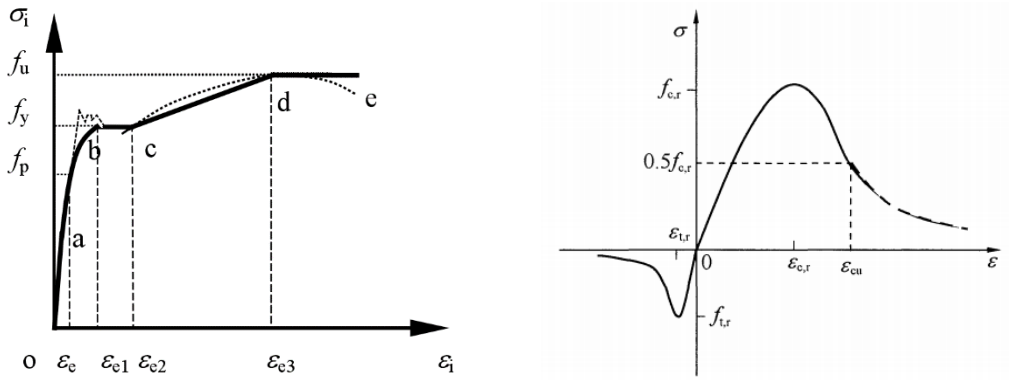

(a) Stress-strain relation model of steel

(b) Stress-strain relation model of concrete

Fig. 13 Stress-strain relation models of steel and concrete

Each component of the joint model is meticulously constructed to match the dimensions of the test specimens. Concrete, steel plates, angle steel, H-shaped steel, studs, and bolts are all simulated using ABAQUS's three-dimensional eight-node reduced integration unit (C3D8R). Steel rebars are simulated using the three-dimensional two-node truss unit (T3D2). To optimize the balance between computational accuracy and efficiency, the mesh size for the steel truss is set at 20mm, while the mesh for other components is set at 30mm.

The steel rebar is first built with line unit, then all rebars are combined into a steel rebar skeleton using the "merge" option of the "Assembly" module of ABAQUS. This steel rebar skeleton is then assigned as a "truss" unit in the "Grid" module of ABAQUS. The steel rebar skeleton is embedded into the concrete slab using the "embedded" command. A detailed contact model is established at the interface of each component to simulate the contact behavior. The main contact interfaces are between: the shear wall steel plate and internal concrete, the shear wall steel plate and concrete slab, the angle steel and concrete slab, the H-shaped steel and concrete slab, the bolt hole and its contact plane, and the support and concrete slab. These contact relationships are defined as "face to face" contact. The tangential behavior between contact surfaces is simulated using a frictional contact, with a friction coefficient of 0.4. The normal behavior between the contact surfaces is simulated using "hard contact". The "Tie" command is used to simplify the welding connections between the shear wall outer steel plate and angle steel, the shear wall steel plates and H-beam steel, the angle steel and bolts, and the H-beam steel and bolts.

To simulate the test's hinged boundary conditions and loading modes, supports and loading beams are positioned at the corresponding positions. Reference points (RP-3 and RP-4) are established on the support plane, constraining the 3-direction translation (U_x, U_y and U_z) and horizontal rotation (R_x). Reference points (RP-1 and RP-2) are established on the plane of the loading beam, and a vertical downward displacement load (U_z) is applied. Given the similarity in the models of the two angle-steel joints (CWSA140 and CWSA120), the specimen CWSA120 is taken as an example. The details of finite element model for specimen CWSA120 are shown in Fig. 14. The details of finite element model of CWH130 are shown in Fig. 15.

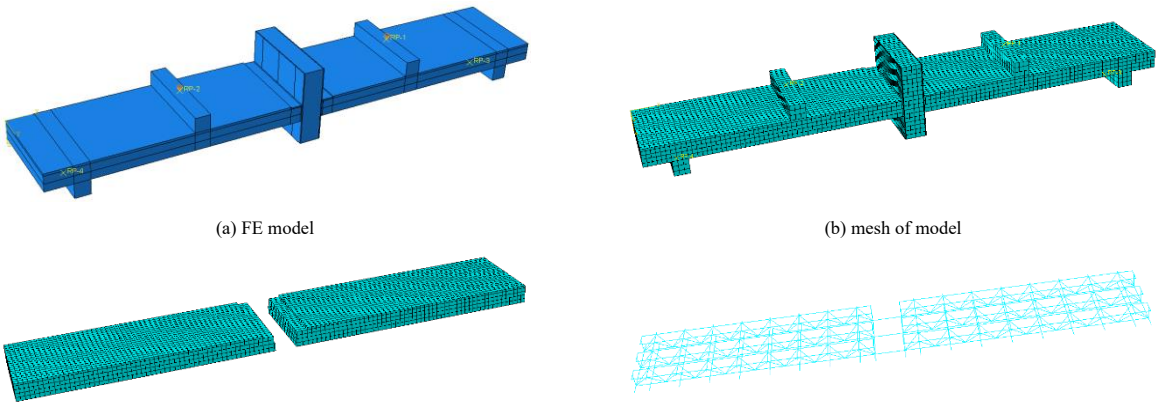

(a) FE model

(b) mesh of model

(c) concrete slab

(d) steel rebar skeleton

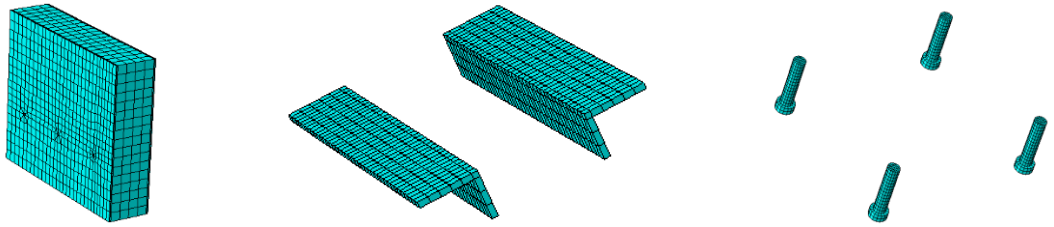

(e) DSC shear wall (f) angle steels (g) shear bolts

Fig. 14 Boundary condition and mesh generation of specimen CWSA120

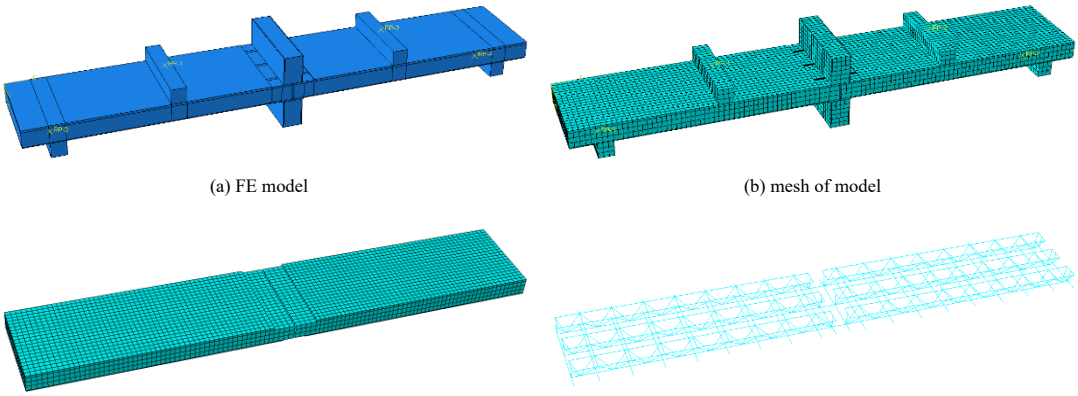

(a) FE model (b) mesh of model

(c) concrete slab (d) steel rebar skeleton

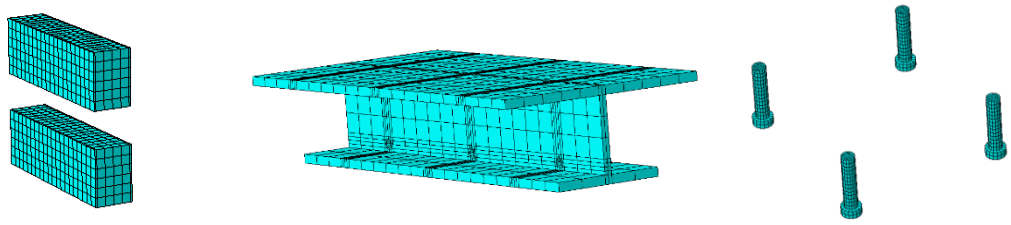

(e) DSC shear wall (f) H-steel (g) shear bolts

Fig. 15 Boundary condition and mesh generation of specimen CWH130

4.2. Results analysis

The bending failure images obtained from the tests of the three specimens were compared to the outcomes of the finite element simulation results (Fig. 16). The three-dimensional finite element models effectively simulated the overall bending failure mode for each specimen. Notably, observations from models CWSA140 andCWSA120 indicate that the highest stresses occur at the angle steel flange in the compression zone of the connection, where cracks also develop between the concrete and the external steel plate of the shear wall in the tension zone. These failure patterns in the joint core area are consistent with experimental observations. Future analysis focused exclusively on the failure of the floor slab' failure reveals that the points of maximum concrete stress in the compression zones of model CWSA140 and specimen CWSA120 are located approximately 100 mm and 150 mm from the load points, respectively, aligning closely with the locations of concrete crushing observed in the experiments. Further examination of model CWH130 shows that the maximum stress occurs at the flange of the H-shaped steel in the compression zone of the joint, with no cracks observed in the concrete of the tension zone—a finding that corroborates the experimental results. The position of maximum compressive stress in the concrete of model CWH130 is observed to be approximately 200 mm from the loading point, which closely matches the concrete crushing locations noted in the experiments. The slab's flexural zone stress could indicate the range of crack development, but the finite element results were unable to accurately predict the location and width of cracks or the crushing phenomenon of the concrete in the top surface of the slab's compression zone. This discrepancy arises primarily attributed to the limitations of the adopted concrete constitutive model, which does not account for the development of concrete cracks and shear transfer.

The load-displacement curves obtained from the finite element analysis (FEA) of the three specimens were compared with the test results, as illustrated in Fig. 17. For specimen CWSA140, the finite element model effectively simulated the specimen's stiffness during the initial loading stage and the bearing capacity at the yield stage but failed to simulate the increase in bearing capacity observed during the later loading stage of loading. For specimens CWSA120 and CWH130, the finite element model effectively simulated the specimens' stiffness at the initial loading stage but was unable to simulate the load decline observed in the tests. The bearing capacities obtained from the FEA for specimens CWSA140, CWSA120, and CWH130 were 49.59kN, 44.86kN, and 48.49kN, respectively. These values represent a decrease of 9.47%, 6.05%, and 1.66% compared to the test results. The discrepancies between the FEA results and the test results is within an acceptable range, supports that the modeling method used in this study accurately reflects the failure mode and bearing capacity of the new assembled wall-slab joints.

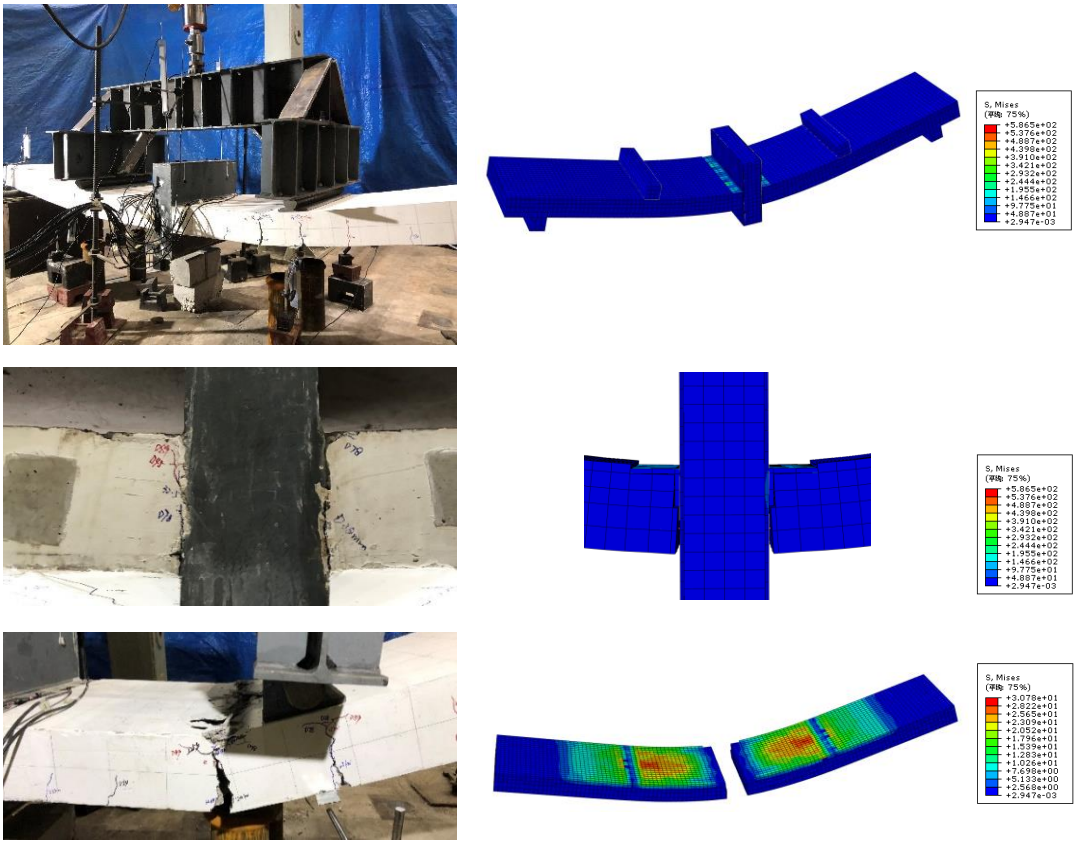

(a) CWSA140

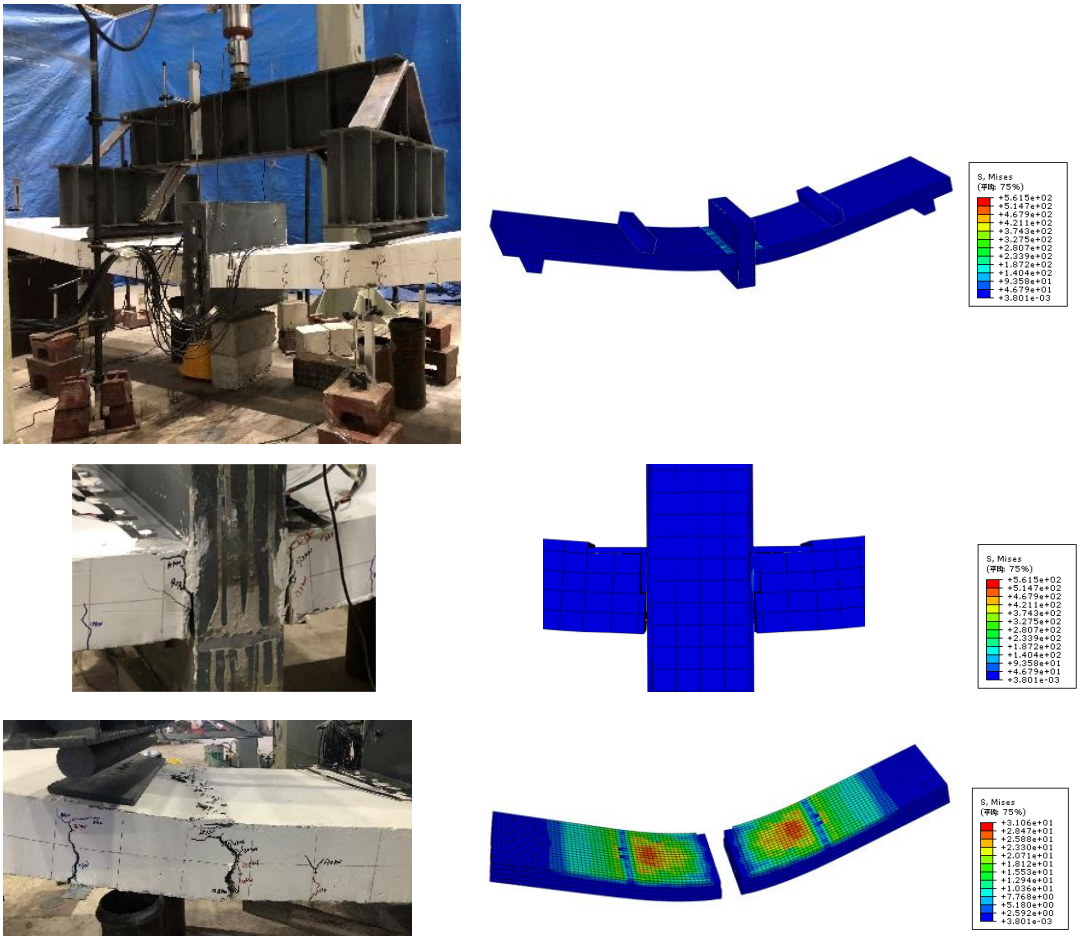

(b) CWSA120

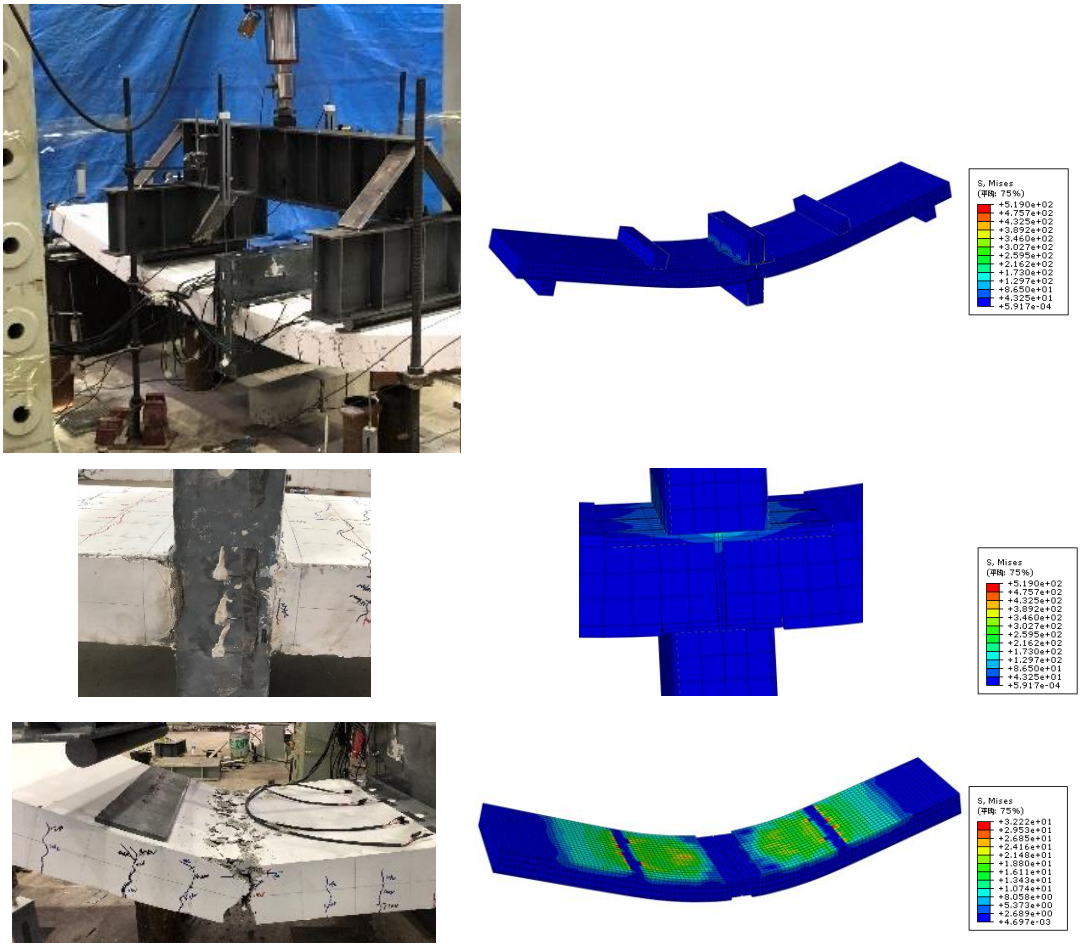

(c) CWH130

Fig. 16 Comparison of the overall deformation of test results and finite element results

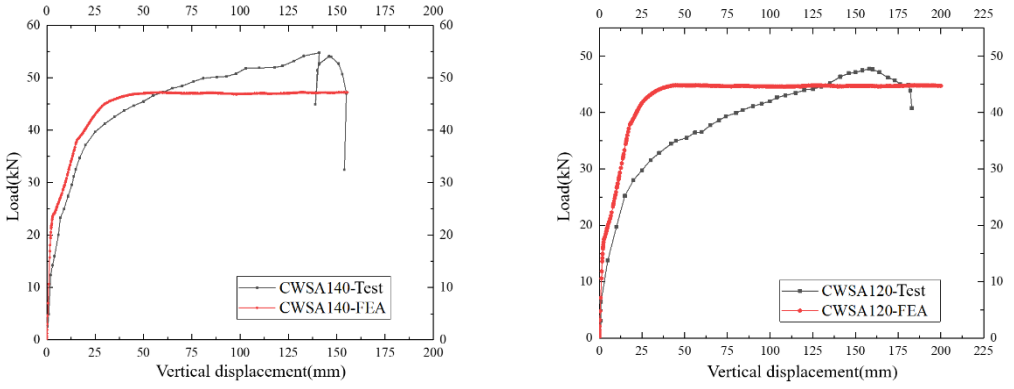

(a) CWSA140 (b) CWSA120

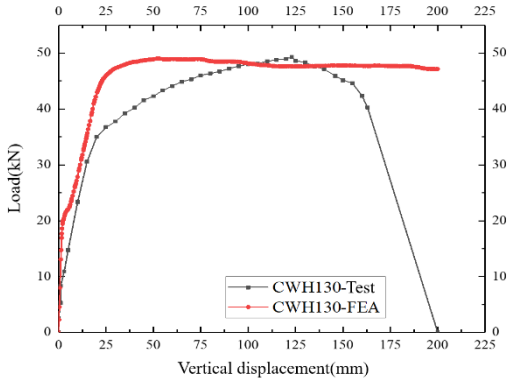

(c) CWH130

Fig. 17 Comparison of load-displacement curves between test specimens and finite element results

5. Calculation of bending capacity

Structural integrity is critically dependent on the performance of connections. A compromised connection can lead to the collapse of an entire structure. The Technical Requirements for Steel Plate Shear Walls [16] and the Code for Seismic Design of Buildings[26], both emphasize the principle of "strong connections and weak members" at shear wall joints. In light of these requirements, the pure bending capacities of two newly assembled wall-slab joints were calculated, adhering to these existing codes. These calculations were conducted to assess the applicability of the current formula to the two newly assembled wall-slab joints. The results serve as a crucial reference for the design of such connections in future projects.

To accurately simulate the stress states of the joint specimens under normal operating conditions, the specimens were inverted during the testing phase. The configuration of the force application is illustrated in Fig. 18. The specimen's bottom supports are hinged, and the vertical load is applied at two quartile points along the specimen. This setup ensures that the section for the specimen between these two loading points is subjected exclusively to a pure bending state.

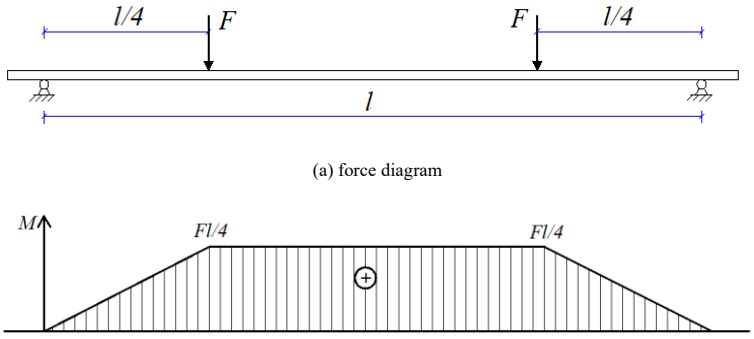

(a) force diagram

(b) bending moment distribution

Fig. 18 The force diagram and bending moment distribution

The relationship between the vertical load (F) and the bending moment (M) of the specimen is expressed as follows:

$$M_{\max} = Fl/4 \quad (4\text{-}1)$$

Failure in specimens typically occurs at the connection positions on the floor slab adjacet to either side of the loading point. As a result, cross-section of the floor slab at these locations is the weakest section when subjected to bending moment loads. To calculate bending moment bearing capacity of these joint specimens, the calculation incorporates the maximum bending moment that the floor slab's cross-section is capable of bearing the bending capacity of the specimens. Fig. 19 illustrates the stress distribution across the floor section when it is subjected to a bending load.

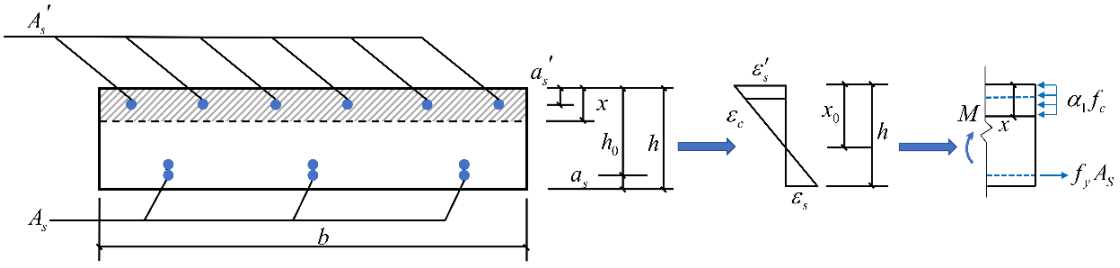

Fig. 19 Calculation diagram of floor cross section under bending moment

According to the cross-section stress balance:

$$\sigma_s A_s = \sigma_s' A_s' + f_c b x \quad (4\text{-}2)$$

The ultimate bending capacity under bending load is obtained as follows:

$$M = \sigma_s A_s (h_0 - a_s') \quad (4\text{-}3)$$

where σ_s and σ_s' are the stresses of longitudinally stressed steel bars in the tension zone and the compression zone, respectively; A_s and A_s' are the section areas of the longitudinal reinforced bars in the tension zone and compression zone, respectively; x is the distance between the edge of compression zone and the point at which the resultant force of the longitudinal reinforcement is applied; h_0 is the effective height of the section; and a_s' is the distance between the application point of longitudinally stressed reinforcement in the compression zone and the edge of the compression zone.

Strain analysis (Fig. 12) demonstrates the longitudinal stressed steel bars (lower rebars of the steel truss) located in the compression zone of the three specimens do not attain the yield strain when subjected to the ultimate load. Consequently, the concrete range of the compression zone cannot be calculated using Eq. (4-2). Conversely, the rebars situated in the joint tension zone do reach the yield stress under the conditions of the yield load. Thus, the specimen's bearing capacity at yield moment and ultimate bending moment can be calculated using the subsequent formula:

Bearing capacity at yield bending moment:

$$M_y = f_y A_s (h_0 - a_s') \quad (4\text{-}4)$$

Bearing capacity at ultimate bending moment:

$$M_p = f_u A_s (h_0 - a_s') \quad (4\text{-}5)$$

A comparison analysis of the calculated and test values is presented in Table. 4. After the vertical bearing capacity (P_y, P_p in Table. 3) is obtained, the yield bending moment (M_y)and ultimate bending moment (M_p) for the test specimens are calculated using Eq. (4-1). This comparison indicates that the error range for the predicted bending capacity of specimens CWSA140 and CWH130 using this calculation method is between 3%-8%. For specimen CWSA120, however, the error ranges from 11% to 20%. Notably, the predicted values for the ultimate bending capacities of all three specimens consistently fall below their test corresponding values. Consequently, it is safe to conclude that the calculation method proposed in this study is a reliable approach for predicting the ultimate bending capacity of the new assembled wall-slab joints for thin double skin composite shear walls and steel truss floor slabs.

Table 4
Bend bearing capacity comparison between the calculated results and test results

Specimens	M_y/(kN·m)	$M_{y,c}$/(kN·m)	M_p/(kN·m)	$M_{p,c}$/(kN·m)	$M_y/M_{y,c}$	$M_p/M_{p,c}$
CWSA140	27.22	26.54	40.13	37.39	1.03	1.07
CWSA120	18.50	20.77	34.98	29.26	0.89	1.20
CWH130	22.59	23.66	36.12	33.32	0.95	1.08

6. Conclusions

This study introduced two newly assembled wall-slab joints f aimed at enhancing the safety of connection between thin double skin composite shear walls and steel truss floor slabs. The mechanical behavior of these joints was evaluated through pure bending tests conducted on three specimens with different connection structures., This evaluation involved test analysis, finite element simulation, and theoretical analyses. The following conclusions were reached:

(1) The two newly assembled wall-slab joints exhibited superior mechanical properties under pure bending load. These joints exhibit reliable structure and excellent force transfer capabilities. The prefabricated floor slabs were identified as the primary failure points under pure bending load, while the joint region remained intact, adhering to the design principle of “strong joint and weak member”. All three specimens developed significant cracking at the loading points of the floor slabs, thus reaching the ultimate load. As a result, the bending capacity of these newly assembled wall-slab joints is predominantly dependent on the flexural performance of the floor slabs. Specifically, the specimens equipped with H-steel joint (CWH130) cracked the latest, exhibiting greater deformation resistance than the other two specimens.

(2) The ABAQUS finite element model proposed in this study effectively simulated the mechanical behavior of the newly assembled wall-slab joints under pure bending loads. The three-dimensional finite element models effectively simulated the entire failure modes for each specimen. Despite the model’s limitation in precisely capturing the crack locations and the concrete crushing phenomena in the compression zones, it accurately predicted the overall bending failure modes.

(3) Considering the failure section of prefabricated floor slab as the weakest section, this study introduces a method to calculate the bending capacity of these joints based on the principle of force balance. The deviations between the calculation results from this formula and the test results were under 20%. The formula's predicted ultimate bending capacities for the three joint specimens were conservative compared to the test values. The calculation method presented in this article provides a dependable foundation for the future engineering design and application of these newly assembled wall-slab joints.

Acknowledgements

The study was sponsored by National Natural Science Foundation of China (No 52278202). The authors acknowledge the financial support and express their gratitude for the support provided by China Construction Science and Industry Corporation Ltd.

References

[1] R.S. Surumi, K.P. Jaya, S. Greeshma. Modelling and Assessment of Shear Wall–Flat Slab Joint Region in Tall Structures. *Arab J Sci Eng*. 40 (2015), 2201–2217.
[2] Y.Q. Shang, W. Ma, X. Li er al. Seismic performance of superposed shear wall- superposed floor slab joints. *Structures*. 60 (2024), 105900.
[3] M.A. Masrom, H.M. Yee, M.E. Mohamed, et al. Seismic performance on stiffness and hysteresis loop of interior wall-slab joint for tunnel form building designs to British standard. *J Fundam Appl Sci*. 9(5S) (2018),75-87.
[4] A. Chalot, N. Roy, L. Michel, et al. Mechanical behavior of a full-scale RC wall-slab connection reinforced with frp under cyclic loading. *Eng Struct*. 239(2021), 112146.
[5] S.R. Salim, J.K. Prabhakaran. Effectiveness of a novel ductile detailing of reinforced concrete wall-flat slab joint. *Aust J Struct Eng*.21(1) (2019), 7–20.
[6] S.C. Chun, T. Ha. Cyclic behavior of wall-slab joints with lap splices of cold-straightened rebars and mechanical splices. *J Struct Eng*.141(2) (2014), 04014101.
[7] A.A.N. Al-aghbari, S.H. Hamid; N.H.A. Hamid, et al. Structural performance of two types of wall slab connection under out-of-plane lateral cyclic loading. *J. Eng. Sci. Technol*. 7(2) (2012), 177–194.
[8] Y.Q. Wang, X. Wang, Y.N. Zhang, et al. Analysis of loading capacity of steel bar truss and concrete superimposed two-way slab. *Journal of Shenyang Jianzhu University (Natural Science)*. 30(3) (2014), 385-391. [in Chinese].
[9] H.J. Wang, H.L. Qian, H.S. Guo, et al. Seismic performance of precast shear wall–slab joint with and without outer longitudinal reinforcement. *Struct Des Tall Special Build*. 30(7) (2021),1-24.
[10] Z.F. Zhu, Z.X. Guo. Seismic test and analysis of joints of new precast concrete shear wall structures. *China Civil Engineering Journal*. 45(1) (2012), 69-76. [in Chinese].
[11] Z.Z. Zhao, J.H. Ke, J.R. Qian, et al. Seismic behavior of cast-in-place reinforced concrete hollow slab-shear wall joints. *Build Struct*.9 (2009), 49-54. [in Chinese].
[12] D. Zenunovic, R. Folic. Models for behaviour analysis of monolithic wall and precast or monolithic floor slab connections. *Eng Struct*. 40 (2012), 466–78.
[13] H.S. Hu, J.G. Nie, M.R. Eatherton. Deformation capacity of concrete-filled steel plate composite shear walls. *Journal of Constructional Steel Research*. 103 (2014) 148–158.
[14] A.H. Varma, S.R. Malushte, K.C. Sener, Z.C. Lai. Steel-plate composite (SC) walls for safety related nuclear facilities: design for in-plane force and out-of-plane moments. *Nuclear Engineering and Design*. 46 (8) (2014), 240–249.
[15] J. Shi, S.Gao, L.H. Guo. Compressive behaviour of double skin composite shear walls stiffened with steel-bars trusses. *Journal of Constructional Steel Research*. 180 (2021),106581.
[16] JGJ/T380-2015: Technical specification for steel plate shear walls. *Ministry of Housing and Urban-Rural Development of the People's Republic of China (MOHURD)*, 2015. [in Chinese].
[17] X. Zhang, Y. Qin, Z. Chen. Experimental seismic behavior of innovative composite shear walls. *Journal of Constructional Steel Research*. 116 (2016), 218–232.
[18] Y. Qin, G.P. Shu, G.G. Zhou, J.H. Han. Compressive behavior of double skin composite wall with different plate thicknesses. *Journal of Constructional Steel Research.* 157 (2019), 297–313.
[19] Y.J. Yu, Y.Q. Luo, S.W. Lin, et al. Experimental seismic behaviors of different connections to CFST end-columns in shear walls. *Journal of Constructional Steel Research.* 196 (2022), 107385.
[20] Z.h. Chen, Z.Y. Zi, T. Zhou, et al. Axial compression stability of thin double-steel-plate and concrete composite shear wall. *Structures*.34 (2021) 3866-3881.
[21] DBJ33/T 1273-2022: Technical specification for double-skin truss-reinforced composite sheer walls. *Zhejiang Provincial Department of Housing and Urban Rural Development,* 2022. [in Chinese].
[22] GB 50010-2010: Code for design of concrete structures. *Ministry of Housing and Urban-Rural Development of the People's Republic of China (MOHURD)*, 2010. [in Chinese].
[23] Z.H. Chen, J. Liu, Ting Zhou, et al. Uniaxial Eccentric-Compression Performance Analysis for Double-Plate Connected Concrete-Filled Steel-Tube Composite Columns. *J. Struct. Eng*.146(8) (2020), 04020161.
[24] Z. Tao, Z.B. Wang, Q. Yu. Finite element modelling of concrete-filled steel stub columns under axial compression. *J. Constr. Steel Res.* 89 (10) (2013),121–131.
[25] A. P. C. Duarte, B. A. Silva, N. Silvestre, et al. Finite element modelling of short steel tubes filled with rubberized concrete. *Compos. Struct.* 150 (8) (2016), 28–40.
[26] GB 50011-2010: code for seismic design of buildings. *Ministry of Housing and Urban-Rural Development of the People's Republic of China (MOHURD)*, 2010. [in Chinese].